Local rift and intraplate seismicity reveal shallow crustal fluid-related activity and sub-crustal faulting

Authors: J. B. Tary[1], R. W. Hobbs[2], C. Peirce[2], C. Lesmes Lesmes[1], M. J. Funnell[2]

[1] Departamento de Geociencias, Universidad de los Andes, Bogotá, Colombia.

[2] Department of Earth Sciences, Durham University, Lower Mountjoy, South Road, Durham, DH13LE, UK.

Corresponding author: Jean Baptiste Tary (jb.tary@uniandes.edu.co)

Departamento de Geociencias

Universidad de los Andes

Cra 1 #18A-12, Bloque M1

Bogotá

Colombia

Highlights

- Seismicity is observed along the Costa Rica Rift in spatial and temporal clusters

- Normal and reverse faulting events are associated with an axial magma lens

- Event clusters associated with fluid-related response of the hydrothermal system

- Intraplate microseismicity is observed around ODP Hole 504B

- Deep events are located at the depth of the brittle-to-plastic transition

1   **Abstract**

2   Seismicity delineating the mid-ocean ridge system in the Panama Basin is mostly concentrated

3   along transform offsets. Most intraplate areas show little-to-no seismic activity. Here we analyze

4   passive recordings from a short-term deployment of 75 ocean-bottom seismographs (OBS) at the

5   Costa Rica Rift (CRR) and across its southern flank along a flowline to Ocean Drilling Program

6   (ODP) Hole 504B. The OBS array recorded 1061 events along the CRR and the Ecuador Fracture

7   Zone, and 127 intraplate events around ODP Hole 504B. The seismic activity along the CRR

8   occurred in clusters, with some events associated with an axial magma lens (AML) located at 3-

9   3.5 km depth below seafloor (bsf), and four events exhibiting normal and reverse faulting focal

10   mechanisms. These deep events are followed by the largest event cluster whose epicenters connect

11   the AML to the seafloor, at a location where a hydrothermal plume was previously reported.

12   During the same period, another event cluster occurs close to the seabed. This spatio-temporal

13   pattern suggests that deeper events close to the AML, which might be related to thermal stresses

14   or stress perturbations due to a volume change in the AML, trigger fluid-related seismicity within

15   the shallower hydrothermal system. The easternmost extent of the seismicity along the CRR

16   corresponds to an overlapping spreading center (OSC). At depth, the seismicity around the OSC

17   is focused beneath one limb, but is spread over a larger area closer to the surface. The focal

18   mechanisms calculated for OSC events show both normal and reverse motions, and might reflect

19   complex stress or fault orientations. Intraplate seismicity around ODP Hole 504B shows both

20   isolated and clustered events from the seafloor to ~15-25 km bsf. Some of this seismicity is likely

21   associated with the reactivation of east-west trending normal faults under high pore pressure and

22   thermoelastic stresses conditions. Deep seismicity (i.e. between 15 and 20 km bsf) occurs in small,

23   well-defined clusters close to ODP Hole 504B, at the theoretical depth of the brittle-to-plastic

24   transition for a ~6.9 Ma oceanic lithosphere. Our results show the importance of short-term OBS

25   deployments for improving our understanding of mid-ocean ridge seismicity and hydrothermal

26   processes, as well as intraplate seismicity and deformation mechanisms.

27

28   Keywords: Mid-ocean ridge seismicity, Hydrothermal processes, Axial magma lens, Intraplate

29   seismicity, Costa Rica Rift, Panama Basin

30

31

32   **1   Introduction**

33   The Panama Basin is located in the eastern part of the Pacific ocean. It is delimited by Central and

34   South America to the north and east, and by the Cocos and Carnegie Ridges to the west and south,

35   respectively (Figure 1). The basin was formed when the Farallon plate separated into the Cocos

36   and Nazca plates during the early Miocene, potentially facilitated by the presence of the Galapagos

37   hotspot (Lonsdale, 2005). The current mid-ocean ridge (MOR) system running through the center

38   of the basin comprises three main ridge segments, namely the Galapagos Spreading Center (GSC),

39   Ecuador Ridge (ER), and Costa Rica Rift (CRR), and three main transform offsets, namely the

40   Inca Transform (IT), Ecuador Fracture Zone (EFZ), and Panama Fracture Zone (PFZ).

41

42   MORs are complex tectono-magmatic systems generally involving intense hydrothermal

43   circulation and high seismic activity (Bohnenstiehl and Dziak, 2009). The characteristics of this

44   seismicity depend on various factors such as the ridge spreading rate and distance off-axis along

45   flowline. Other aspects include: i) the maximum event depth, controlled by the brittle-to-plastic

46   transition which is deeper at ridges with lower spreading rates due to their lower heat budget; ii)

47   the size of the seismogenic zone which, following the 750-800ºC isotherm (Searle and Escartín,

48   2004), increases with lithospheric age (Wiens and Stein, 1984; Engeln et al., 1986); and iii) the

49   stress regime which changes with distance from the rift neovolcanic zone, being extensional close

50   to the rift zone to become compressional further away from it (Bergman and Solomon, 1984).

51

52   This study focuses on one MOR segment within the Panama Basin, the CRR, and its southern

53   flank along a flowline to the site of the Ocean Drilling Program (ODP) Hole 504B (Becker et al.,

54   1989), located in ~6.9 Ma lithosphere at a distance of ~240 km from the CRR (Figure 1). The

55   CRR, located between the EFZ and the PFZ, is characterized by current asymmetric and

56   intermediate half-spreading rates of ~21-24 mm/yr and 39-41 mm/yr on its north and south sides,

57   respectively (Wilson et al., 2019). During its 11 Myr history, the CRR has oscillated between

58   magmatic and magma-dominated crustal formation regimes corresponding to changes in full

59   spreading rate of between 50 and 72 mm/yr (Wilson et al., 2019). The amount of tectonic stretching

60   and magma supply, therefore, vary not only over time but also spatially along the CRR (Wilson et

61   al., 2019; Robinson et al., 2020). An axial magma lens (AML) exists in the central part of the CRR

62   at the depth of ~3.0-3.5 km bsf (Buck et al., 1997; Lowell et al., 2020). The AML is a ~6-km long,

63   localized feature which appears to be associated with hydrothermal circulation and seismicity

64   (Lowell et al., 2020). Approximately 5-10 km along the CRR to the east of the AML, a small

65   overlapping spreading center (OSC) is also present. This OSC appears to mark the boundary

66   between two currently magmatically-distinct parts of the CRR; the western spreading limb having

67   a higher magmatic supply relative to the eastern (Robinson et al., 2020). Most of the seismicity

68   inventoried by the USGS in the Panama Basin is concentrated along transform ridge offsets with

69   relatively few intraplate events (Figure S1). Spreading segments in the basin, including the CRR,

70   appear to be mostly aseismic in global earthquake catalog terms.

71

72   MORs are generally characterized by low magnitude seismicity (M<4) which requires the

73   deployment of local temporary ocean-bottom seismograph (OBS) networks for accurate seismic

74   monitoring (e.g., Grevemeyer et al., 2019). In this study, we use a deployment of 75 OBSs with a

75   short inter-instrument spacing (5-9 km in two grids and along one profile) during the RRS James

76   Cook cruise JC114 (Hobbs & Peirce, 2015) (Figure 1), as well as the availability of local 3D

77   velocity models (Robinson et al., 2020; Gregory, 2018), to obtain high precision seismicity

78   location and focal mechanisms. The diversity of structures observed at the CRR (e.g., the AML

79   and OSC), and the quality of the information collected over the years in this area by successive

80   cruises to both the CRR and ODP Hole 504B, allow us to investigate the microseismicity's spatio-

81   temporal distribution, including the seismic activity of the CRR itself and its relationship with

82   hydrothermal circulation and the presence of the AML, the seismo-tectonic expression of the OSC,

83   and the intraplate seismic activity in relatively young oceanic crust (~6.9 Ma) close to ODP Hole

84   504B.

85

86

87   **2   Data and network**

88   The at-sea part of the OSCAR (*O*ceanographic and *S*eismic *C*haracterization of heat dissipation

89   and alteration by hydrothermal fluids at an *A*xial *R*idge) research project took place in January and

90   February, 2015, with data acquisition taking place from both the RRS James Cook (JC112, JC113

91   and JC114) and the FS Sonne (SO238). Two of the main objectives of these cruises were to study

92   the structure of the oceanic crust, including the ridge axis and its flank (i.e., from an age of 0 Ma

93   to ~6.9 Ma), and to investigate the relationship between tectonic features, fluid fluxes and heat

94   transfer between the oceanic crust and the ocean. To address these objectives:

95   i)   a comprehensive physical oceanography survey of the whole basin was undertaken during

96   JC112 (Banyte et al., 2018a; Banyte et al., 2018b);

97   ii) heat flow measurements were acquired during JC113 (Kolandaivelu et al., 2020; Lowell et

98   al., 2020); and

5

99   iii) multichannel seismic (MCS) reflection profiles, wide-angle (WA) seismic profiles, sub-

100   bottom profiler (SBP) profiles, swath bathymetry, and potential field data were acquired

101   during JC114 (Hobbs & Peirce, 2015; Wilson et al., 2019; Gregory, 2018; Robinson et al.,

102   2020; Haughton et al., 2020).

103   Even though the OBSs were originally deployed for active-source WA seismic acquisition, they

104   recorded continuously throughout deployment, including during gaps between active-source

105   profiling. In this study we focus on the analysis of the OBS passive seismic recordings.

106

107   The OBSs were deployed in two grid-form arrays and along one 2D transect (Figure 1). From

108   north to south, a grid of 25 OBSs were deployed at the CRR (hereafter called "North Grid" or NG),

109   25 OBSs were deployed following a flowline from the NG to ODP Hole 504B (hereafter called

110   SAP as in synthetic aperture profile), and 25 OBSs were deployed around ODP Hole 504B

111   (hereafter called "South Grid" or SG). The OBSs in the different arrays also have different

112   recording durations between January 25, 2015, to February 28, 2015 (see Hobbs & Peirce (2015)

113   for details). All OBSs had a three-component, short-period (4.5 Hz) geophone pack and a

114   hydrophone, with data sampled at 500 Hz. The clock drift of each OBS was linearly corrected

115   using GPS synchronization at deployment and recovery.

116

117

118   **3   Methods**

119   **3.1. Microseismicity location**

120   Using the continuous time series (band-pass filtered between 5 and 120 Hz), we first detected

121   potential events using the STA/LTA technique (short-term average/long-term average). Events

122   were then automatically extracted that exceeded a minimum STA/LTA threshold of 2 within a

123   window of 10 s and if they were recorded by a minimum of three stations. The automatically-

124   generated detections were then manually reviewed to retain only earthquakes (micro or otherwise).

125   For the events selected, we then picked P- and S-waves, and attributed picking uncertainties

126   automatically based on the signal-to-noise ratio (SNR). Absolute event locations were obtained

127   with NonLinLoc using a non-linear, grid-search method (Lomax et al., 2009). Only events with at

128   least six picks were included in the location determination (see Table S1 for the main input

129   parameters). Any additional processing for the event locations and velocity model selection are

130   described separately for the North and South Grids in the sections below. After locating the events,

131   moment magnitudes were estimated automatically using the Brune fit on S-wave spectra after

132   instrumental response removal (Eaton et al., 2014).

133

134   ### 3.2. North Grid

135   Most seismicity recorded by the NG instruments is located within ~100 km of the grid. A detailed

136   3D P-wave velocity model obtained using seismic tomography analysis of the WA seismic data is

137   available for the grid area centered on the CRR (Robinson et al., 2020). We therefore used

138   Robinson et al.'s (2020) 3D velocity model in NonLinLoc for all events falling within the OBS

139   grid footprint to a depth below sea surface <12 km. Care was given to the depth of the OBSs within

140   this 3D velocity model (given the node spacing) so that they lay on the seafloor and not in the

141   water column.

142

143   For all other events recorded by the NG OBSs that lie outside the grid footprint, we used a 1D

144   velocity model derived from the 3D P-wave velocity model, corresponding to the near-axis

145   structure of the CRR (Figure 8 of Robinson et al., 2020). Individual travel-time tables were

146   calculated for each OBS to account for their respective depths. We employ a V_p/V_s ratio of 1.8 to

147   calculate S-wave travel-time tables. This estimate comes from the work of Gregory (2018) at the

148   SG and other studies from other ridges (e.g., Collier and Singh, 1998 – Poisson's ratio of between

7

149 0.27 and 0.31) which together provide a generalistic estimate of ~0.28 (hence Vp/Vs ratio of 1.8).

150 A negligible amount of sediment is present close to the CRR and so no sediment layer is present

151 in either velocity model used for the NG event analysis.

152

153 ### 3.3. South Grid

154 The NG procedure was adopted, with most seismicity recorded within ~100-200 km from the SG.

155 An equivalent 3D P-wave velocity model is also available for the SG which is centered on ODP

156 Hole 504B (Gregory, 2018). However, in the SG case most events were either too deep or located

157 outside the area of the 3D velocity model. We therefore used an average 1D version of the 3D

158 velocity model to locate all events which, at a crustal scale, does not significantly misrepresent the

159 modelled velocities. To calculate S-wave travel-times we use a V_p/V_s ratio of 1.76 as defined by

160 Gregory (2018). Although ODP Hole 504B logs (Cann et al., 1983) record a sediment thickness

161 of ~275 m, the 1D model includes this layer as a 300 m-thick low-velocity layer ($V_p \approx 1.68$ km/s)

162 to be consistent with the node spacing of the Gregory (2018) 3D model.

163

164 ### 3.4. Focal mechanism calculation

165 As the origin of the many analyzed events, especially close to the CRR, could involve the presence

166 and migration of hydrothermal fluids or magma, we assume that they correspond mainly to fault

167 rupture and can be represented by double-couple sources, with small non-double components due

168 to these fluids (e.g., Wilcock et al., 2009; Waldhauser & Tolstoy, 2011). For focal mechanism

169 calculations we select only events with at least 16 phase picks. Following this criteria, 63 events

170 were analyzed for the NG, and 13 events for the SG. Time series were generally band-pass filtered

171 between 5 and 50 Hz prior to polarity picking. The orientation of the OBS vertical component was

172 first checked using the active-source seismic shots. Only clear P-wave polarities picked on the

173   vertical component were included. The same 1D velocity models and V_p/V_s ratios as described

174   above were used for focal mechanism calculations. We also fixed the NonLinLoc event locations

175   in these calculations. Finally, we used FOCMEC (e.g., Snoke, 2003), part of the SEISAN

176   distribution (Havskov & Ottemöller, 1999), to calculate the focal mechanisms. All solutions were

177   obtained using a 0 to 2 polarity error (Table S2). To verify the robustness of the solutions obtained,

178   we also calculated the solutions with FPFIT (Reasenberg and Oppenheimer, 1985) to check their

179   consistency, and progressively removed different polarities from the calculation to quality control

180   the results. FPFIT also provides uncertainties on the nodal planes (Table S2). In the following

181   section we present focal mechanism solutions that are consistent and well-constrained by their set

182   of polarities.

183

184

185   **4   Results**

186   **4.1.   North Grid**

187   After microearthquake selection, 1061 events were detected for the short recording period of the

188   NG (from January 25 to February 17, 2015). In total this represents 3409 P-wave picks and 3433

189   S-wave picks. Of these 1061 events, 459 events were located using the 3D velocity model, 218

190   events were located with the 1D velocity model, and 384 events had less than six phases and were

191   not located (Figures 2 and S2). Locations in 1D and 3D have average root-mean square residuals

192   in travel-time of 0.19 and 0.07 s, respectively. For location using the 3D velocity model, horizontal

193   uncertainties range mainly between 0.5 and 10.0 km (with a distribution up to ~30 km representing

194   ~15% of the events), and vertical uncertainties between 2.2 and 6.0 km. These locations, close to

195   the NG instruments, are well-constrained (Figure 2). For location using the 1D velocity model,

196   horizontal uncertainties range mainly between 5.0 and 26.5 km with a relatively even distribution,

197   and vertical uncertainties range between 7.5 and 30.0 km. These locations have higher

198   uncertainties for two main reasons: i) a smaller number of phase picks for some events located

199   close to the NG array; and ii) their larger distance from the NG array (Figure 2). Estimated event

200   moment magnitudes range mainly between 0.1 and 3.1, with events from the CRR having small

201   magnitudes mainly between 0.1 and 1.7, and the events from the EFZ having higher magnitudes

202   mainly between 2.1 and 3.1. The highest magnitude event (M_w 4.3) located is from the EFZ.

203

204   Most events are clustered in specific areas centered on the main tectono-magmatic features of the

205   area. Some events are associated with a recent splay of the EFZ that might represent an eastward

206   jump in its location. The smaller number of events for this structure is likely related to its larger

207   distance from the NG, such that only higher magnitude events exceed the detection threshold.

208   Closer to the NG, events are aligned along the CRR with all seismicity apparently located west of

209   the non-transform discontinuity. We do not believe that this is an artifact of the OBS array location

210   as events have been recorded originating as far as the PFZ, but it could be a function of the short

211   recording window which may have just captured a period of active seismicity along the western

212   CRR. Most individual clusters are contained within areas a few kilometers in width and elongated

213   in depth, with positions ranging from the seafloor to ~7 km, the base of the oceanic crust (Figure

214   3). These clusters are defined based on their spatial proximity, although some clusters also have

215   events with high waveform similarity, especially Cluster 6 (Figure 4). For the NG events, the well-

216   constrained focal mechanisms are shown in Figure 3. Events with focal mechanisms located

217   outside the NG are less well constrained than those inside the network due to the small aperture of

218   the polarities on the focal sphere. We present the best constrained focal mechanism for which a

219   relatively small number of polarities seem to control the orientation and position of nodal planes

220   (Figure 2). It shows a predominantly normal fault mechanism but with a strike-slip component.

221   However, the focal mechanisms of all events within the NG show both normal and reverse focal

222 mechanisms. In general, the main mode (i.e., normal or reverse) is well constrained by the

223 polarities even if the plane orientations vary (Table S2 and Figures S3 and S4).

224

225 On February 10, 2015, approximately 140 events were detected mainly in two clusters located

226 along the CRR (indicated by numbers 1 and 6 on Figures 3, 4 and 5). Cluster 1 extends from the

227 seafloor to a depth of ~3 km bsf, while Cluster 6 is concentrated close to the seafloor (i.e., from

228 the seafloor to a depth of 0.5-1.0 km). For Clusters 1 and 6 no well-constrained focal mechanisms

229 could be determined. The event clusters located to the side of and slightly deeper than Cluster 1

230 have both normal and reverse focal mechanisms (Clusters 2 and 3 on Figure 3). Focal mechanisms

231 of Cluster 2 show both normal and reverse solutions with varying plane orientations. For Cluster

232 3, the only well-constrained event (depth ~2.4 km bsf) has a reverse focal mechanism with a small

233 strike-slip component. Two events located close to the OSC (Cluster 4) show normal and reverse

234 focal mechanisms. Finally, one event belonging to a deeper cluster below, at approximately 5.4

235 km bsf, has a normal focal mechanism with a small strike-slip component.

236

237 **4.2. South Grid**

238 For the SG recording period (from February 3 to February 28, 2015), 127 seismic events were

239 detected corresponding to 606 and 652 P- and S-wave picks, respectively (e.g., Figure 6). Of these

240 127 events, 98 have at least six phase picks and were located (Figures 7 and S2). These locations

241 have an average root-mean square residual in travel-time of 0.12 s. Horizontal uncertainties range

242 mainly from 2.0 to 30.0 km and vertical from 2.5 to 20.0 km with a higher proportion of events

243 with uncertainties between 17.0 and 20.0 km. The larger uncertainties obtained for the SG, when

244 compared with the NG, are due to the larger distances between array and location in general for

245 the SG. In fact, most events are located outside the SG array, and are much deeper. Similar to the

246　NG, event magnitudes range mainly from 0.8 to 2.9, with higher magnitude events generally

247　corresponding to events further away from the network.

248

249　Seismicity around the SG is not as clustered as it is for the NG even though the events often occur

250　in small groups of ~2-3 events spaced closely in time. In this area both shallow and deep seismicity

251　is present including many events associated with horizontal and vertical uncertainties of less than

252　±5 km. Shallow seismicity (i.e., between 0 and 5 km bsf) is distributed throughout most of the SG,

253　sometimes in small clusters. Deep seismicity is mainly situated below the SG and to the southeast.

254　In the southeast, the events seem related to the presence of a north-south fracture zone that

255　intersects with the Carnegie Ridge.

256

257　Overall, in the SG region the deep seismicity shows both individual events and small clusters.

258　Deep events in the range 20-30 km bsf is anomalous for ~6.9 Ma oceanic crust (Searle and Escartín,

259　2004). However, these events are within the OBS network and many have a large number of P-

260　and S-wave picks (>15 picks, up to 37 picks) and, hence, small uncertainties (e.g., Figure 7). The

261　main factor influencing the depth of these events is the velocity model. In this area close to ODP

262　Hole 504B, the crustal velocity structure is laterally homogeneous (Gregory, 2018) so velocity

263　heterogeneities within the crust cannot explain the anomalous depth of these events. The deeper

264　velocity structure is less well constrained than in the shallower crust, so there is a trade-off between

265　the estimated velocity and event depth, where decreasing the velocity would result in shallower

266　events. Assuming that the first OBS to record the event presented in Figure 6 is located almost

267　vertically above the hypocenter, travel-time differences in a one-layer over a half-space model can

268　be used to investigate crustal and event depths following

269
$$T_w - T_p = \left[\left(\frac{h_1}{V_{w1}} + \frac{h_2}{V_{w2}} \right) - \left(\frac{h_1}{V_{p1}} + \frac{h_2}{V_{p2}} \right) \right],$$

270   where T_w and T_p are travel-times of a specific wavetrain and the primary P-wave, respectively, h_1

271   and h_2 correspond to the first layer thickness (i.e., the oceanic crust) and the depth of the event

272   below h_1 (i.e., in the upper mantle), and V_w and V_p are average seismic velocities of the specific

273   wavetrain and P-waves. Using time series from OBS 17, we observe three main wavetrains, the P-

274   wave, followed by a high-amplitude wavetrain, and the S-wave. The travel-time difference

275   between the high-amplitude wavetrain and the P-wave is ~0.7 s which, using average seismic

276   velocities from the 1D velocity model and assuming this high-amplitude wavetrain is a P-to-S

277   conversion at the base of the oceanic crust, gives an oceanic crust thickness h_1 of ~6 km. This is

278   consistent with the 3D velocity model of Gregory (2018).

279

280   The travel-time difference between P- and S-waves for OBS 17 (see Figure 1 for location) is ~1.8

281   s. This travel-time difference corresponds to an event depth of ~17.5 km bsf, slightly shallower

282   than the depth of 20.9 km obtained by the 1D event location. This difference is likely related to

283   unmapped velocity model variations below the oceanic crust, such as a lower seismic wave

284   velocity in the upper mantle than that assumed (V_{p2} of 8 km/s) (Figure S5). Two events which

285   occurred within a 10 min time interval show similar strike-slip focal mechanisms. Another event

286   located spatially close-by exhibits an oblique normal fault mechanism with a significant strike-slip

287   component.

288

289

290   **5   Discussion**

291   **5.1. Seismic activity along the CRR and EFZ**

292   An intense period of seismic activity is observed along the CRR during a temporary local OBS

293   deployment. This seismicity is dominated by small events with magnitudes below ~2. This

13

294 provides a very different view of the CRR compared to that offered by the seismicity recorded by

295 seismological networks onshore. East of the OBS deployment, no detectable microearthquakes

296 were located which implies that no event of magnitude >2 occurred during the recording period.

297 Hence, we conclude that over the short-term there is a strong difference in seismic activity between

298 the western and eastern parts of the CRR, although this might not be representative of the medium-

299 to long-term activity of the CRR. We hypothesize that the higher seismic activity in the western

300 part might reflect the focus of current magmatic activity along the CRR (Vargas et al., 2018;

301 Robinson et al., 2020; Lowell et al. 2020). The well-located microseismicity is mostly limited to

302 the first 7 km bsf corresponding to the brittle part of the oceanic crust (Searle and Escartín, 2004).

303

304 Within the OBS network, the microseismicity is focused in specific clusters along the CRR

305 (Figures 2 and 3). The most significant seismic activity is observed above and around the AML.

306 Cluster 1 is located above the western end of the AML with depths ranging from the AML itself

307 to the seafloor. The position of this cluster is close to the position of a large hydrothermal plume

308 detected in the water column (Lowell et al., 2020). The spatio-temporal pattern of this cluster

309 suggests that deeper events close to the AML, which might be related to thermal stresses or stress

310 perturbations due to a volume change in the AML, trigger fluid-related seismicity within the

311 shallower parts of the hydrothermal system (e.g., Sohn et al., 1999; Wilcock et al. 2009). Similarly,

312 Cluster 6 is located on the CRR between the seafloor and a depth of ~0.5-1.0 km. Even though no

313 bathymetric feature was observed close to this cluster, it might be associated with hydrothermal

314 circulation closer to the surface through a process of thermal cracking for example (Tolstoy et al.,

315 2008). Cluster 2, situated at the same depth level as the AML, exhibits a lower event density and

316 both normal and reverse focal mechanisms. The number of focal mechanisms is limited but they

317 do not show plane orientations consistent with MOR-perpendicular extension only. Other factors

318 such as thermal stresses due to hydrothermal circulation, and stress perturbations due to the

14

319   presence of the AML (i.e., inflation and diking events), must play a role in the generation of these

320   events (Wilcock et al., 2009; Waldhauser and Tolstoy, 2011). The lower event density could, in

321   turn, be related to higher temperatures closer to the AML, locally weakening the crust and

322   promoting aseismic deformation.

323

324   Events from Cluster 2 occur mostly during the first week of the recording period, while events

325   from Clusters 1 and 6 occur mostly during the last two weeks (Figure 5). The timing between

326   Cluster 2 and Clusters 1 and 6, as well as the crisis-like character of Clusters 1 and 6 (i.e., ~140

327   events in one day), suggest that a deep magmatic event led to fluid-triggered seismicity from AML

328   depth to the surface. The approximate time lag and distance between the clusters at depth close to

329   the AML and cluster 1, are 3 days and 3.5 km, respectively. Considering a possible pore pressure

330   diffusion between these clusters, the diffusion timescale in an isotropic poroelastic medium is

331   given by $\tau = L^2/D$ (L the characteristic diffusion distance and D the hydraulic diffusivity) (Manga

332   and Wang, 2007) which corresponds to a hydraulic diffusivity of ~50 m^2/s in our case. The

333   formation permeability k can be obtained from $k = \mu\xi D$, with μ the dynamic viscosity and ξ the

334   storage compressibility (e.g., Davis et al., 2004). Assuming similar parameter values as Davis et

335   al. (2004), for the hydrothermal system of the Juan de Fuca ridge ($\mu = 10^{-4}$ Pa.s and $\xi =$

336   2.27×10^{-10} Pa^{-1}), a hydraulic diffusivity of 50 m^2/s corresponds to a permeability of ~10^{-12} m^2.

337   These values are within the range of possible values for young oceanic crust close to the ridge axis

338   (e.g., Davis et al., 2004; Barreyre et al., 2018; Crone et al., 2011).

339

340   The OSC on the CRR is relatively small with an offset between limbs of ~1.5 km and an overlap

341   of ~2.5 km. The overlap-to-offset ratio is ~1.6:1 which is different from that of 3:1 observed at

342   other ridges (e.g., MacDonald et al., 1987). This leads Robinson et al. (2020) to suggest that this

343 OSC might still be developing. If the magma supply to the western limb is larger than to the

344 eastern, as the observed microseismicity and other observations seem to indicate (e.g. Robinson et

345 al., 2020), the western limb of the OSC might be undergoing a phase of expansion that will

346 eventually decapitate the eastern limb (MacDonald et al., 1987). Robinson et al. (2020) modelled

347 a low P-wave velocity associated with the OSC, which they interpret as being due to a porosity

348 increase caused by fracturing. Using gravity data modelling, they also suggest that a high-density

349 anomaly is present below the OSC which could be attributed to either a thinner or denser oceanic

350 crust. We observe some relatively sparse seismic activity with event depths from the surface to ~7

351 km bsf, approximately corresponding to the base of the oceanic crust (Figures 3 and S2). At depth,

352 between 5 km and 7 km bsf, the events are focused in the center of the OSC while, closer to the

353 surface, the events are spread over the center and both limbs. These observations suggest that the

354 deformation associated with this OSC extends throughout the entire oceanic crust, favoring the

355 scenario of a denser oceanic crust at depth as best explaining the observed gravity anomaly.

356 Deformation at depth below the OSC might then be localized along one main structure.

357

358 Outside the OBS network, further along the CRR, the located microseismicity is mostly clustered.

359 This suggests, again, that this microseismicity is associated with hydrothermal circulation, either

360 occurring throughout the entire oceanic crust for the cluster to the west of the OBS network, or

361 focused near the surface for the small cluster closer to its intersection with the EFZ (Figures 2 and

362 S2). Along the EFZ, most of the microseismicity recorded during this deployment is located along

363 the eastern flank and shallower than 5 km-depth bsf and, although poorly constrained, focal

364 mechanisms suggest right lateral strike-slip (Figures S2a, S3 and S4).

365

366   **5.2. Intraplate seismicity close to ODP Hole 504B**

367   Microseismicity around ODP Hole 504B occurs along a north-south trending fracture zone that

368   runs parallel to the PFZ (Lonsdale, 2005), and spans a depth range from the seafloor to ~30 km

369   bsf (Figure 7). There are a number of potential causes of the intraplate seismicity observed around

370   the SG:

371   • seismic reflection profiles (Kent et al., 1996; Gregory, 2018; Wilson et al., 2019) and a

372   seismic anisotropy study (Gregory, 2018) show that the crust to the south of the CRR is

373   crossed by roughly east-west trending ridge-parallel normal faults. These studies also show

374   that these faults are currently active and may serve as fluid pathways and, hence, could

375   generate microseismicity. These faults continue for at least a few kilometers into the

376   basement, but their actual true depth extent is unknown (Gregory, 2018);

377   • the cluster of deep microseismicity to the southeast of the grid is consistent with the

378   microseismicity around ODP Hole 504B reported by Lonsdale (2005) that occurs along a

379   north-south trending fracture zone that runs parallel to the PFZ and spans a depth range

380   from the seafloor to ~30 km bsf;

381   • the sub-Moho events within the grid between depths of 10-25 km maybe the result of

382   thermoelastic stresses due to lithospheric cooling causing the reactivation of faults. This

383   would lead to an event concentration below the Moho (at ~5-6 km depth bsf, Gregory,

384   2018) to the depth of the 750-800ºC isotherm (Bergman & Solomon, 1984);

385   • the origin of a second, deep cluster within the grid at a depth of ~15-20 km bsf is more

386   enigmatic. It appears to be located at the maximum depth of brittle-to-plastic transition

387   based on predicted depth of 20±5 km for the 750-800°C isotherm for a 6.9 Ma oceanic

388   plate (e.g., Parker & Oldenburg, 1973; Wiens & Stein, 1984; Searle and Escartín, 2004).

389   These deep events, therefore, occur at the limit of oceanic intraplate seismicity (e.g., Wiens

390   & Stein, 1983). This may imply that there has been a deepening of the mechanical behavior

391   transition, which could occur in response to enhanced cooling of the lithosphere by

392   hydrothermal circulation, higher pore pressures (though its cause would be difficult to

393   explain), or an elevated strain rate (Wiens & Stein, 1983; Wiens & Stein, 1984). If there

394   has been a deepening of the transition zone then the observation from seismic anisotropy

395   analysis suggests the presence of open fractures in the basement (Gregory, 2018), which

396   could facilitate enhanced hydrothermal circulation and cooling. It should be noted that the

397   fact that this seismicity appears as a localized cluster may be the result of the short period

398   of acquisition.

399

400   Two focal mechanisms were obtained for these deep events within the footprint of the SG network

401   and show mainly strike-slip solutions. The nodal planes of these solutions agree with the

402   southwest-northeast regional maximum horizontal principal stress orientation (Kent et al., 1996).

403   The observed microseismicity shows no direct evidence of the influence of the nearby Nazca plate

404   subduction below the South-American plate.

405

406   A key question is: does this seismicity represent the reactivation of pre-existing structures or are

407   some new ones forming at the brittle to ductile transition? Models of crustal formation at an

408   intermediate-rate spreading mid-ocean ridge involve the generation of crustal scale faults that

409   penetrate to the brittle-ductile transition, bounding the neo-volcanic zone and accommodating the

410   subsidence of the ridge flanks due to cooling (Searle and Escartín, 2004). However, lithospheric

411   cooling implies a thickening of the brittle lithosphere lid with age (Wiens and Stein, 1984; Engeln

412   et al., 1986) and these original faults could grow downwards to keep pace with this thickening.

413   Some seismicity would be associated with these new fault extensions that link to the pre-existing

414   faults. An alternative would be that these are entirely new structures initiated, for example, by

415   thermal state differences between younger and older portions of the lithosphere adjacent to each

416   other. On the flanks near to the ridge, normal faulting is the dominant mechanism while at more

417   distal locations the stress field will become dominated by the regional plate tectonic stresses, as

418   we have observed around the site of ODP 504B. Resolution of this issue requires a dedicated long-

419   term deployment of OBSs over a ridge flank to monitor earthquake activity.

420

421

422   **6   Conclusion**

423   Using a short-term local deployment of 75 OBSs in the Panama Basin, we present an analysis of

424   the microseismic activity along the CRR and around ODP Hole 504B. The high seismic activity

425   along the CRR occurs episodically in clusters and is limited to its western and central parts. This

426   clustering might be related to the increased magmatic activity in these areas. In the central part of

427   the CRR, the primary clusters seem closely related with the presence of the AML. Many events

428   are located between the surface and AML depth where a hydrothermal plume has been detected.

429   Events located at AML depth (~3.0-4.0 km bsf), with normal and reverse fault focal mechanisms,

430   are most likely related to stress perturbations due to hydrothermal fluids or AML volumetric

431   change. This is consistent with a scenario of a deep magmatic event triggering fluid-related

432   responses in the shallower hydrothermal system, as has been observed on the Juan de Fuca ridge

433   (Wilcock et al., 2009) and the East Pacific Rise (Waldhauser and Tolstoy, 2011).

434

435   Lower seismic activity is observed around the OSC. This third-order discontinuity is the boundary

436   between the western and eastern segments of the CRR, and corresponds to the eastern limit of the

437   microseismicity along the CRR. Some microseismicity is present throughout the entire oceanic

438   crust below the OSC, with deeper events focused at its center and shallower events spread along

439   the OSC. We interpret this observation as relating to one principal structure located deep below

19

440　the OSC which dissipates into multiple structures in the shallower part. No clear pattern in focal

441　mechanism is observed suggesting that this zone has complex stress or fault geometries.

442

443　Around ODP Hole 504B, microseismicity is observed but with a much lower incidence when

444　compared to the western part of the CRR. The depths of this microseismicity range from the

445　seafloor to ~20 km bsf. Here, the microseismicity within the brittle part of the oceanic lithosphere

446　might be associated with active east-west trending normal faults. High pore pressures as well as

447　thermoelastic stresses might lead to the reactivation of these faults. Deeper seismicity between ~15

448　and 20 km bsf below the SG could be located at the brittle-to-plastic transition (i.e. the 750-800ºC

449　isotherm). Higher pore pressures, cooling through hydrothermal circulation, and strain rates in this

450　area could, however, deepen the brittle-to-plastic transition, together with the crust here being

451　generated during a period of magmatic accretion rather than magma-dominated tectonic extension.

452　Whether these events occurred on pre-existing structures or due to another cause remains an open

453　question.

454

455　This study shows the importance of local OBS deployments as short-term surveys to monitor the

456　seismic activity of offshore structures which exhibit microseismicity of low magnitude (<4). It

457　also shows how they can be used to improve our understanding of tectonic and hydrothermal

458　processes occurring at MORs, and that intra-plate deformation does occur in regions previously

459　thought to be tectonically quiescent.

460

461

References

Banyte, D., Morales Maqueda, M. A., Smeed, D. A., Hobbs, R., Megann, A., & Recalde, S. (2018a). Geothermal Heating in the Panama Basin: 1. Hydrography of the Basin. *Journal of Geophysical Research: Oceans*, *123*(10), 7382-7392.

Banyte, D., Morales Maqueda, M. A., Smeed, D. A., Megann, A., Hobbs, R., & Recalde, S. (2018b). Geothermal Heating in the Panama Basin. Part II: Abyssal Water Mass Transformation. *Journal of Geophysical Research: Oceans*, *123*(10), 7393-7406.

Barreyre, T., Olive, J.-A., Crone, T. J., & Sohn, R. A. (2018). Depth-dependent permeability and heat output at basalt-hosted hydrothermal systems across mid-ocean ridge spreading rates. *Geochemistry, Geophysics, Geosystems*, 19.

Becker, K., Sakai, H., Adamson, A. C., Alexandrovitch, A., Alt, J. C., et al. (1989). Drilling deep into young oceanic crust, Hole 504B, Costa Rica Rift. *Rev. of Geophysics*, *27*, 79-102.

Bergman, E. A., & Solomon, S. C. (1984). Source Mechanisms of Earthquakes Near Mid-Ocean Ridges. In: Body Waveform Inversion: Implications for the Early Evolution of Oceanic Lithosphere. *Journal of Geophysical Research*, *89*(B13), 11415-11441.

Bohnenstiehl, D. R., & Dziak, R. P. (2009). Mid-ocean ridge seismicity. In Cochran, J. K., Bokuniewicz, H. J., & Yager, P. L. (Eds.), *Encyclopedia of Ocean Sciences* (3rd Edition), Academic Press, Oxford.

Buck, W. R., Carbotte, S. M., & Mutter, C. (1997). Controls on extrusion at mid-ocean ridges. *Geology*, *25*, 935-938.

Cann, J.R., Langseth, M.G., Honnorez, J., Von Herzen, R.P., White, S.M., et al. (1983). Initial Reports of the Deep Sea Drilling Project, 69, Initial Reports of the Deep Sea Drilling Project. *U.S. Government Printing Office*. https://doi.org/10.2973/dsdp.proc.69.1983

Collier, J. S., & Singh, S. C. (1998), Poisson's ratio structure of young oceanic crust, *J. Geophys. Res.*, 103(B9), 20981– 20996, doi:10.1029/98JB01980.

Crone, T. J., M. Tolstoy, & Stroup, D. F. (2011), Permeability structure of young ocean crust from poroelastically triggered earthquakes. *Geophys. Res. Lett.*, 38, L05305.

Davis, E., Becker, K., Dziak, R., Cassidy, J., Wang, K., & Lilley, M. (2004). Hydrological response to a seafloor spreading episode on the Juan de Fuca ridge. *Nature*, 430(6997), 335-338.

Eaton, D. W., van der Baan, M., Birkelo, B., & Tary, J. B. (2014). Scaling relations and spectral characteristics of tensile microseisms: evidence for opening/closing cracks during hydraulic fracturing. *Geoph. J. Int.*, *196*, 1844-1857.

Engeln, J. F., Wiens, D. A., & Stein, S. (1986). Mechanisms and Depths of Atlantic Transform Earthquakes. *Journal of Geophysical Research*, *91*(B1), 548-577.

Gregory, E. P. M. (2018). *The seismic characterisation of layer 2 in oceanic crust around ODP borehole 504B* (PhD thesis). University of Durham, UK.

Grevemeyer, I., Hayman, N. W., Lange, D., Peirce, C., Papenberg, C., Van Avendock, H. J.A., Schmid, F., Gómez de la Peña, L., & Dannowski, A. (2019). Constraining the maximum depth of brittle deformation at slow- and ultraslow-spreading ridges using microseismicity. *Geology*, *47*, 1069-1073.

Haughton, G., Murton, B. J., Hobbs, R., Wilson, D., & Zhang, L. (2020). Correlating seafloor tectonic and magmatic features at the Costa Rica and Ecuador spreading ridge segments. submitted.

Havskov, J., & Ottemöller, L. (1999). SEISAN earthquake analysis software. *Seismological Research Letters*, *70*, 532–534.

Hobbs, R., & Peirce, C. (2015). RRS James Cook JC114 Cruise Report. Online Report. https://www.bodc.ac.uk/resources/inventories/cruise_inventory/reports/jc114.pdf

Kolandaivelu, K. P., Harris, R. N., Lowell, R. P., Robinson, A.H., Wilson. D. J., & Hobbs, R. W. (2020). Evolution of heat flow, hydrothermal circulation and permeability on the young southern flank of the Costa Rica Rift. *Geoph. J. Int.*, *220*, 278–295.

Lomax, A., Michelini, A., & Curtis, A. (2009). Earthquake location, direct, global-search methods. In Encyclopedia of complexity and system science, part 5 (p. 2449–2473). New York: Springer.

Lonsdale, P. (2005). Creation of the Cocos and Nazca plates by fission of the Farallon plate, *Tectonophysics*, *404*, 237-264.

Lowell, R. P., Zhang, L., Maqueda, M. A. M., Banyte, D., Tong, V. C. H., et al. (2020). Magma-hydrothermal interactions at the Costa Rica Rift from data collected in 1994 and 2015. *Earth and Planetary Science Letters*, *531*, 115991.

MacDonald, K. C., Sempere, J.-C., Fox, P. J., & Tyce, R. (1987). Tectonic evolution of ridge-axis discontinuities by the meeting, linking, or self-decapitation of neighboring ridge segments. *Geology*, *15*, 993-997.

Manga, M., & Wang, C.-Y. (2007). Earthquake hydrology. In: G. Schubert (ed.), Treatise on Geophysics, 4, Elsevier, Amsterdam, 293-320.

Minshull, T.A., Sinha, M. C., & Peirce, C. (2005). Multi-disciplinary, sub-seabed geophysical imaging. *Sea Technology*, 46, 27-31.

Parker, R. L., & Oldenburg, D. W. (1973). Thermal Model of Ocean Ridges. *Nature, 242*, 137-139.

Reasenberg, P., and D. Oppenheimer (1985). FPFIT, FPPLOT and FPPAGE: FORTRAN computer programs for calculating and displaying earthquake fault-plane solutions, *U.S. Geol. Surv. Open File Rept.*, 85-739.

Robinson, A. H., Zhang, L., Hobbs, R. W., Peirce, C., & Tong, V. C. H. (2020). Magmatic and tectonic segmentation of the intermediate-spreading Costa Rica Rift – a fine balance between magma supply rate, faulting, and hydrothermal circulation. *Geoph. J. Int.*, *222*, 132–152.

Searle, R. C., & Escartín. J. (2004). The Rheology and Morphology of Oceanic Lithosphere and Mid-Ocean Ridges. In Mid-Ocean Ridges (Eds. C. German, J. Lin and L. Parson). doi:10.1029/148GM03.

Snoke, J. A. (2003). FOCMEC: FOcal MEChanism determinations. In International Handbook of Earthquake and Engineering Seismology (Eds. W. H. K. Lee, H. Kanamori, P. C. Jennings, and C. Kisslinger), Academic Press, San Diego.

Sohn, R. A., Hildebrand, J. A., & Webb, S. C. (1999). A microearthquake survey of the high-temperature vent fields on the volcanically active East Pacific Rise (9º 50'N). *Journal of Geophysical Research*, *104*(B11), 25367-25277.

Tolstoy, M., Waldhauser, F., Bohnenstiehl, D. R., Weekly, R. T., & Kim, W.-Y. (2008). Seismic identification of along-axis hydrothermal flow on the East Pacific Rise, *Nature*, *451*, 181-184.

Vargas, C. A., Pulido, J. E., & Hobbs, R. W. (2018). Thermal structure of the Panama Basin by analysis of seismic attenuation. *Tectonophysics*, *730*, 81-99.

Waldhauser, F., & Tolstoy, M. (2011). Seismogenic structure and processes associated with magma inflation and hydrothermal circulation beneath the East Pacific Rise at 9º50'N. *Geochem. Geophys. Geosyst.*, *12*(9), Q08T10.

Wiens, D. A., & Stein, S. (1983). Age dependence of oceanic intraplate seismicity and implications for lithospheric evolution. *Journal of Geophysical Research: Solid Earth*, *88*(B8), 6455-6468.

Wiens, D. A., & Stein, S. (1984). Intraplate seismicity and stresses in young oceanic lithosphere. *Journal of Geophysical Research: Solid Earth*, *89*(B13), 11442-11464.

Wilcock, W. S. D., Hooft, E. E. E., Toomey, D. R., McGill, P. R., Barclay, A. H., et al. (2009). The role of magma injection in localizing black-smoker activity. *Nature Geoscience*, *2*, 509-513.

Wilson, D. J., Robinson, A. H., Hobbs, R. W., Peirce, C., & Funnell, M. J. (2019). Does intermediate spreading-rate oceanic crust result from episodic transition between magmatic and magma-dominated, faulting-enhanced spreading?–The Costa Rica Rift example. *Geoph. J. Int.*, *218*, 1617–1641.

Figures
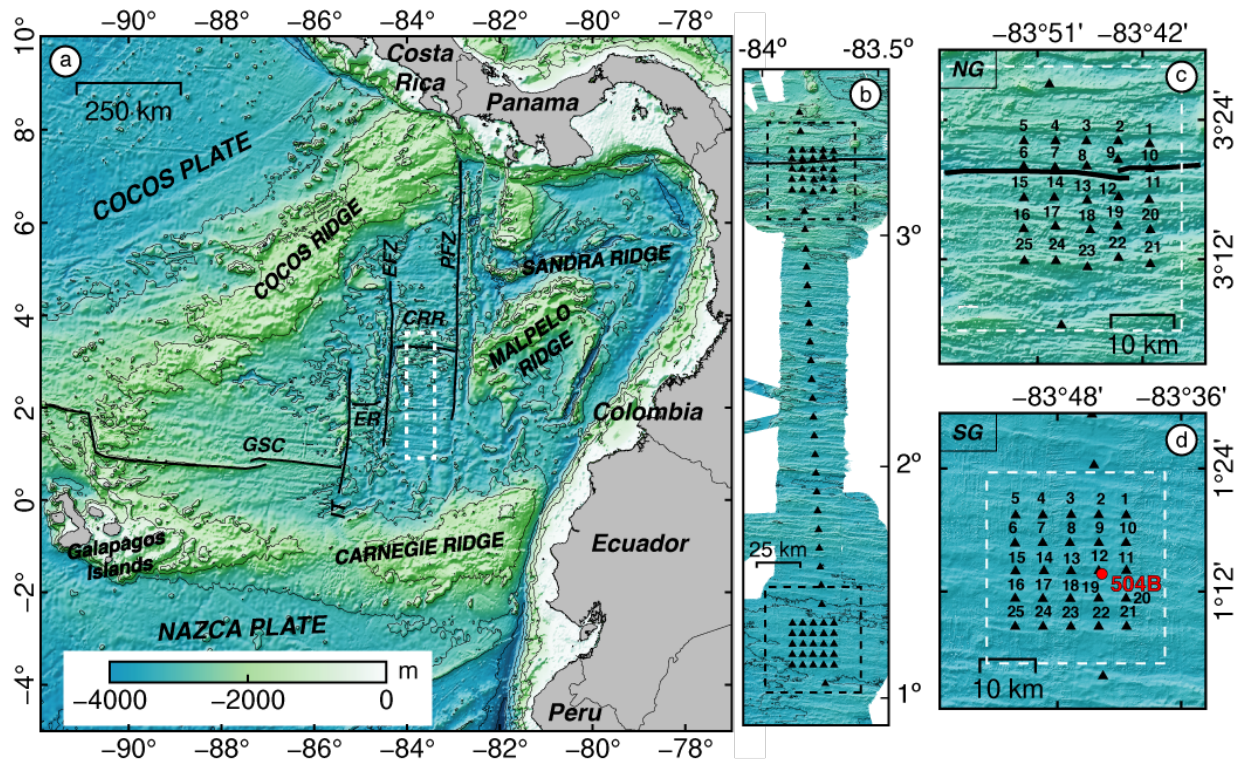
Figure 1. a) Bathymetric map of the Panama Basin delimited by the Cocos and Carnegie Ridges. Spreading centers (CRR - Costa Rica Rift, ER - Ecuador Ridge, GSC - Galapagos Spreading Center) and transform faults (PFZ - Panama Fracture Zone, EFZ - Ecuador Fracture Zone, IT – Inca Transform) are indicated. b) Map of the ocean-bottom seismographs deployed (black triangles) during JC114, corresponding to the dashed white rectangle in a). c) and d) Maps of the North (NG) and South (SG) Grids, respectively, corresponding to the black dashed rectangles in b). Dashed white rectangles indicate zones covered by 3D velocity models, and ODP Hole 504B is indicated by the red dot.
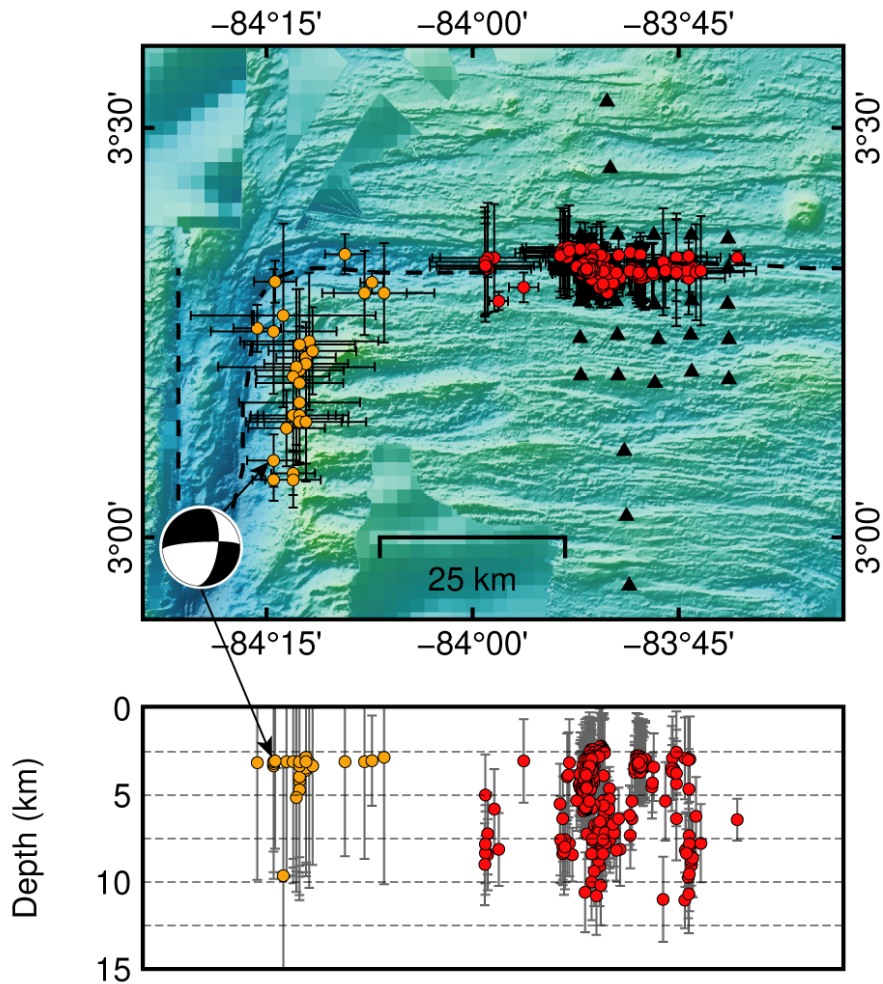
Figure 2. NG microearthquake locations showing only events with horizontal uncertainties <±15 km and vertical uncertainties <±7.5 km for those located outside the network, and with horizontal uncertainties <±7.5 km and vertical uncertainties <±2.5 km for those located inside the network. Microearthquakes located with the 1D and 3D velocity models correspond to the orange and red dots, respectively. Black triangles indicate the OBS positions. Error bars correspond to event uncertainties calculated from the best-fit ellipsoid of the probability density function of each event.
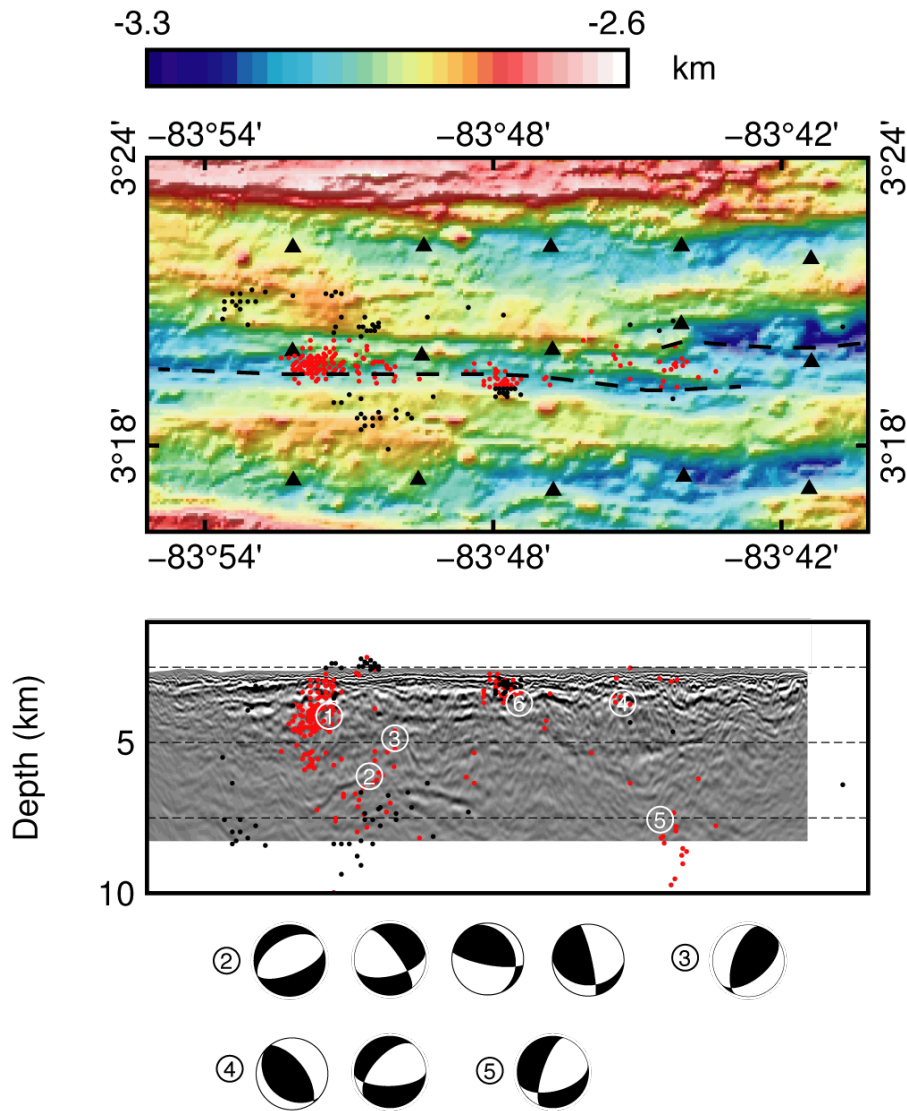
Figure 3. (Top) Bathymetric map and microearthquake locations (in and outside the axial valley by red and black dots, respectively) of the NG at the CRR (ridge axis trend dashed black line). Black triangles correspond to OBS positions. (Bottom) East-west cross-section superimposed on the depth migrated MCS profile NG_Bb13 of Lowell et al. (2020). Numbers correspond to different clusters and example focal mechanisms are shown below.
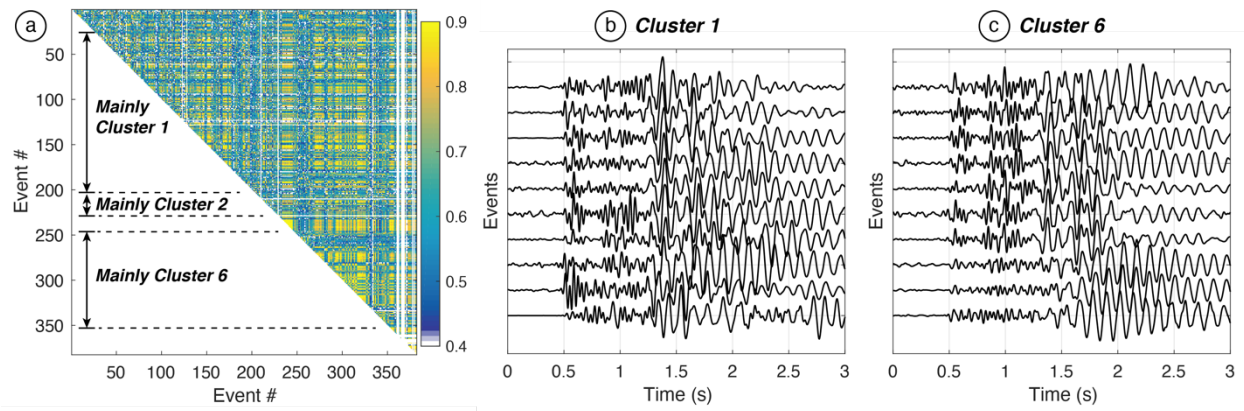
Figure 4. a) Full waveform cross correlation coefficients between events on Figure 3 (OBS 7, vertical component, band-pass filtered between 5 and 20 Hz). b) and c) Time series examples of events belonging to Clusters 1 and 6 (see Figure 3), respectively. Data from the vertical component OBS 7 (see Figure 1 for location), band-pass filtered between 5 and 30 Hz.
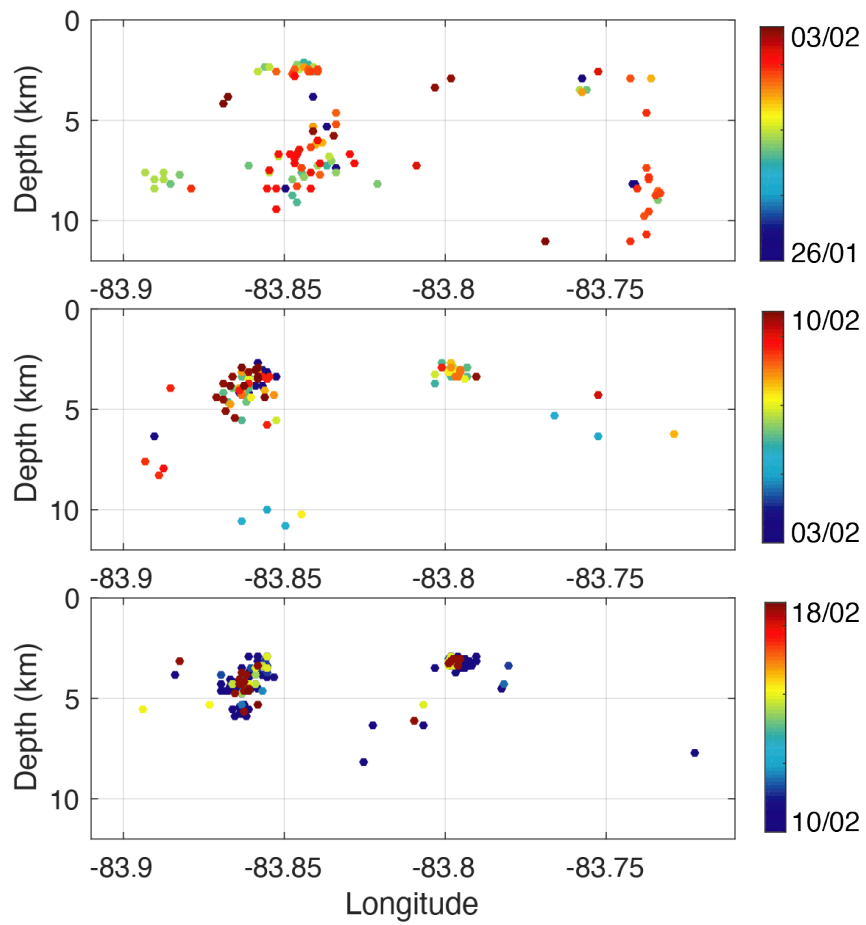
Figure 5. Cross-sections of NG microearthquake locations around the CRR, color-coded depending on event date in 2015 from the beginning (top) to the end (bottom) of the deployment.
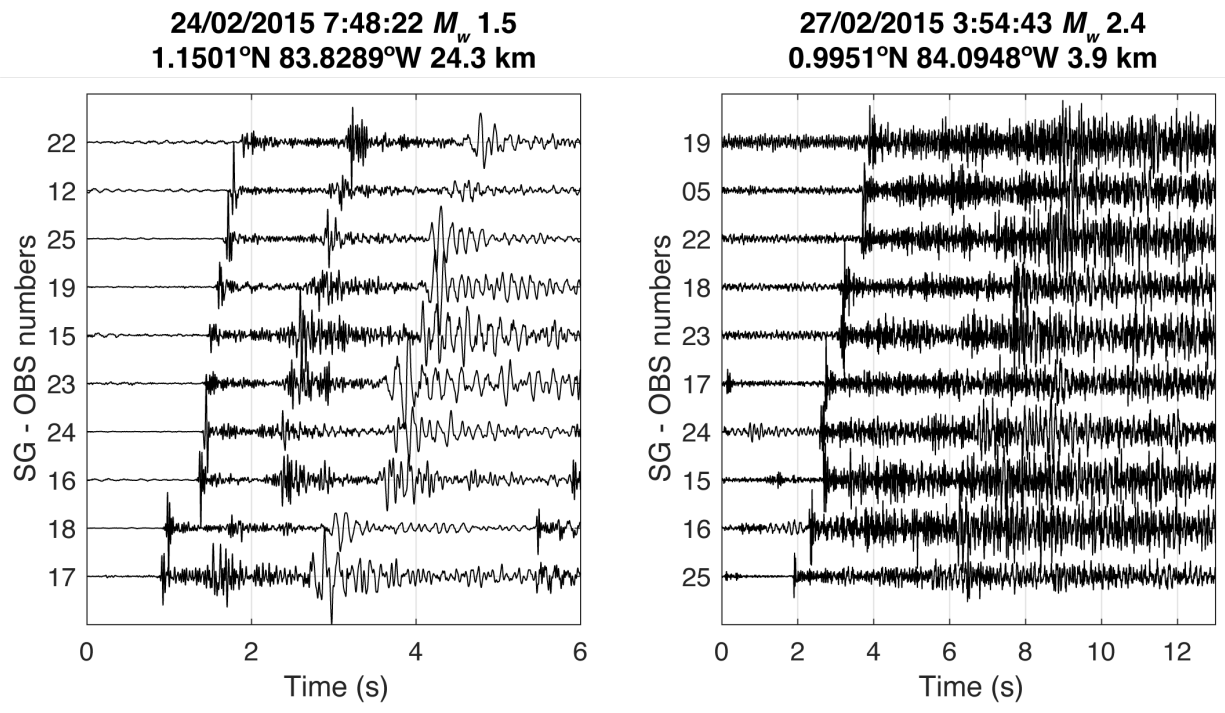
Figure 6. Time series of two microearthquakes recorded by the SG at a selection of 10 OBSs (vertical component, band-pass filtered between 5 and 50 Hz). See Figure 1 for OBS location.
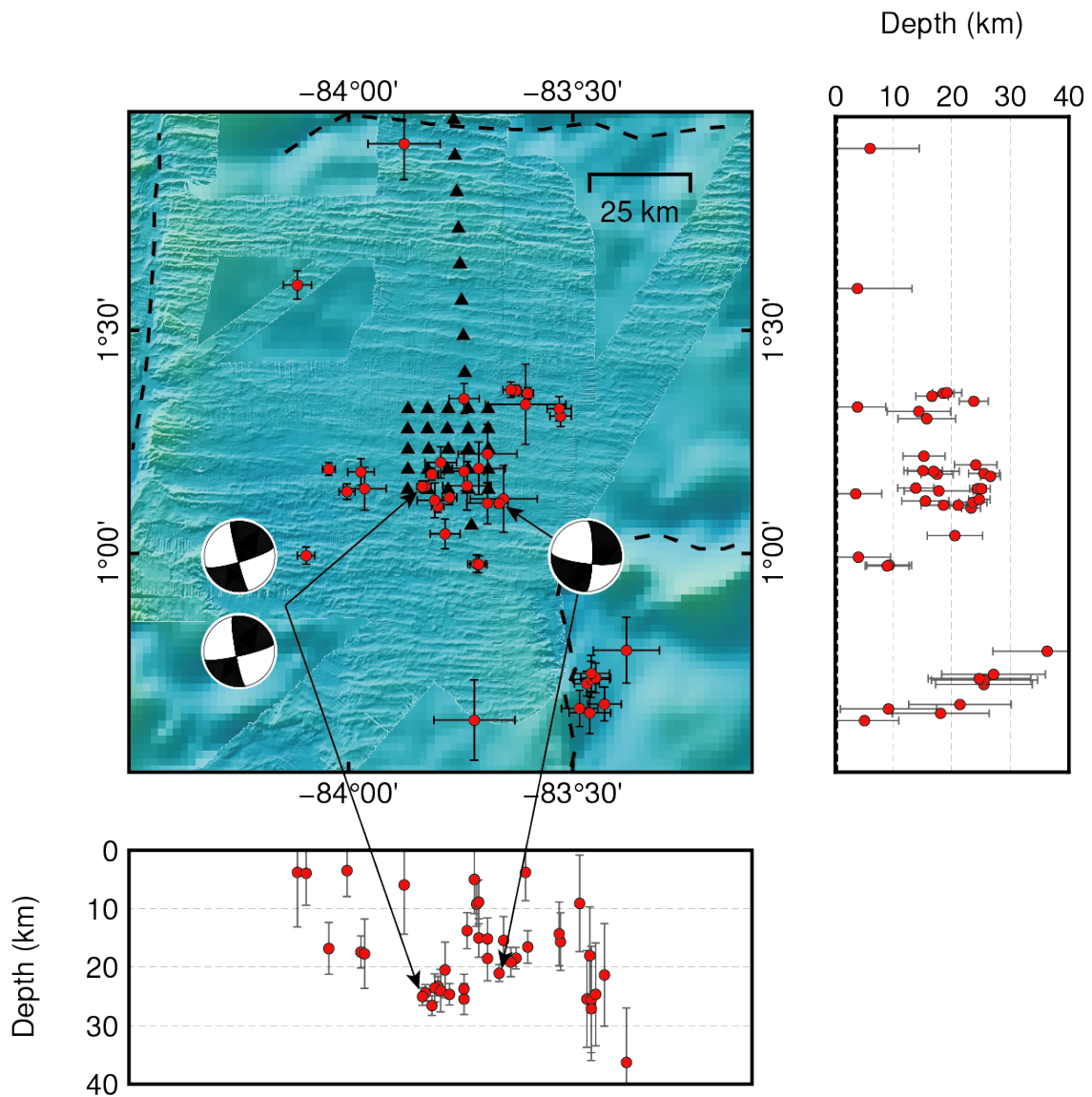
Figure 7. SG microearthquake locations showing only events with horizontal and vertical uncertainties <±10 km. Black triangles indicate the OBS positions. Error bars correspond to event uncertainties calculated from the best-fit ellipsoid of the probability density functions of each event. Focal mechanisms are shown for example deep events.

Supplementary information

For

Local rift and intraplate seismicity reveal shallow crustal fluid-related activity and sub-crustal faulting

By J. B. Tary, R. W. Hobbs, C. Peirce, C. Lesmes Lesmes, M. J. Funnell

Table S1. Main input parameters used for the three NonLinLoc microseismicity locations. NG = North Grid, SG = South Grid.

	NG - 3D velocity model	NG - 1D velocity model	SG - 1D velocity model
Grid size (x, y, z)	60 x 60 x 12 km	1400 x 1400 x 60 km	580 x 580 x 38 km
Grid node spacing (x, y, z)	0.1 x 0.1 x 0.1 km	0.2 x 0.2 x 0.2 km	0.2 x 0.2 x 0.2 km
Grid-search algorithm	Oct-Tree	Oct-Tree	Oct-Tree
Likelihood function	Equal differential-time	Equal differential-time	Equal differential-time
Minimum phase number	6	6	6

Table S2. Location and focal mechanism characteristics of events with well-resolved solutions. Mw: moment magnitude estimations. RMS: average root-mean-square misfits in travel time. Er. H: horizontal uncertainties. Er. Z: vertical uncertainties. # polarities: number of P-wave polarities used for focal mechanism calculation. Polar. Errors: number of polarity errors in focal mechanism calculation. ΔStrike, ΔDip, ΔRake: uncertainty estimates in strike, dip and rake calculated by FPFIT.

NG															
Time	Longitude	Latitude	Depth	Mw	RMS	Er. H	Er. Z	Strike	Dip	Rake	# Polarities	Polar. Errors	Δ Strike	Δ Dip	Δ Rake
Jan 26, 2015 16:24:21	-83.837	3.327	2.4	1.2	0.13	0.5	1.4	199	52	69	17	2	5	5	2
Jan 29, 2015 11:08:39	-84.241	3.094	0.4	3.9	0.16	3.6	6.1	267	77	-40	6	0	4	4	10
Jan 30, 2015 07:51:07	-83.758	3.331	0.6	0.8	0.14	0.8	2.5	131	30	80	11	1	10	14	15
Jan 31, 2015 13:18:38	-83.838	3.329	3.2	0.8	0.11	0.7	1.6	68	55	-84	8	1	50	10	20
Jan 31, 2015 14:20:42	-83.758	3.330	0.8	0.8	0.11	0.5	1.6	89	54	-59	11	0	7	1	1
Feb 01, 2015 06:17:50	-83.842	3.328	3.5	1.0	0.11	0.6	1.1	325	67	-46	12	1	1	1	4
Feb 01, 2015 10:40:55	-83.741	3.326	5.4	0.7	0.08	0.5	1.4	76	41	-41	8	0	8	9	10
Feb 01, 2015 16:21:07	-83.847	3.327	4.2	1.1	0.11	1.5	2.8	101	76	69	13	2	5	4	15
Feb 01, 2015 20:57:54	-83.845	3.330	3.6	1.1	0.10	1.9	3.1	92	31	17	13	0	2	3	22
SG															
Feb 24, 2015 07:48:22	-83.829	1.150	20.9	1.5	0.23	1.4	1.4	165	84	14	10	1	9	6	4
Feb 24, 2015 07:58:28	-83.835	1.150	21.6	1.4	0.24	1.4	1.5	169	80	12	11	1	5	3	56
Feb 24, 2015 15:10:18	-83.664	1.113	17.6	1.6	0.18	1.1	1.5	1	74	-20	11	1	5	5	2
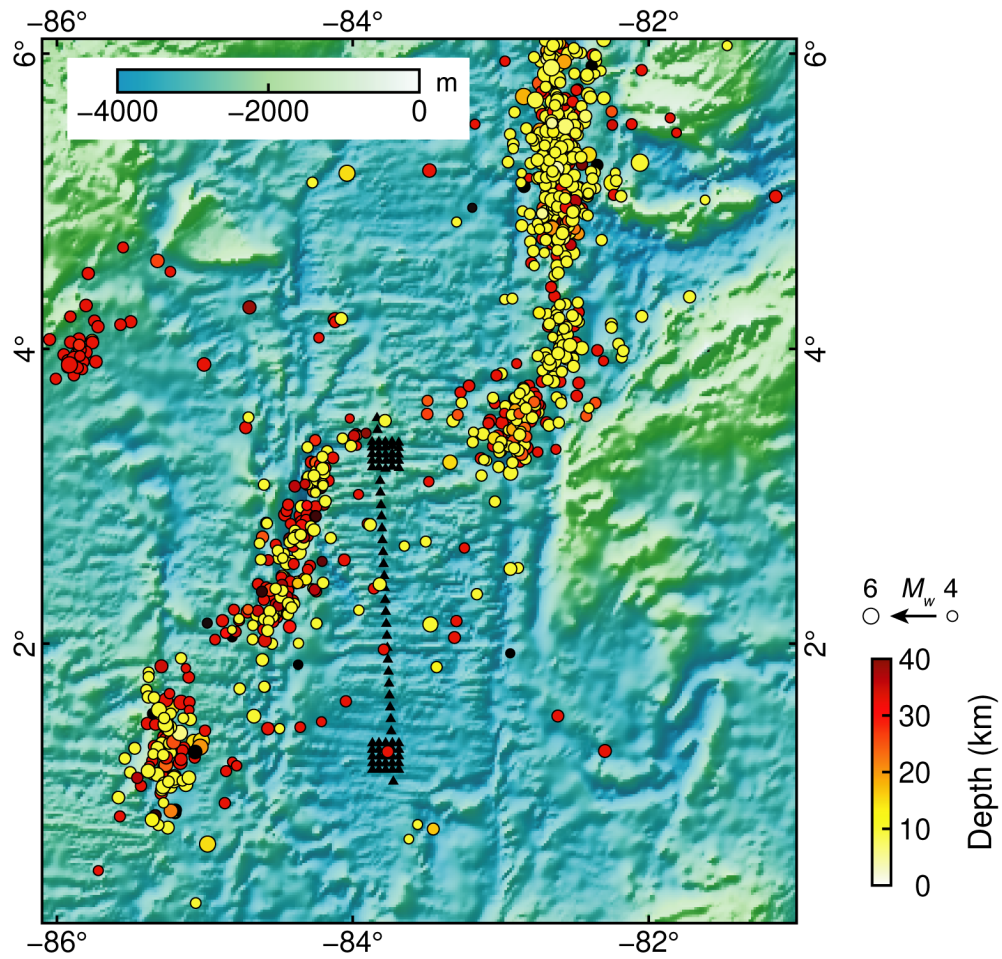
Figure S1. Seismicity between 1927 and 2020 in the central part of the Panama Basin, as inventoried by the USGS. Events are color-coded depending on their depth and their symbol size indicates their magnitude. Black triangles show OBSs deployed during cruise JC114.
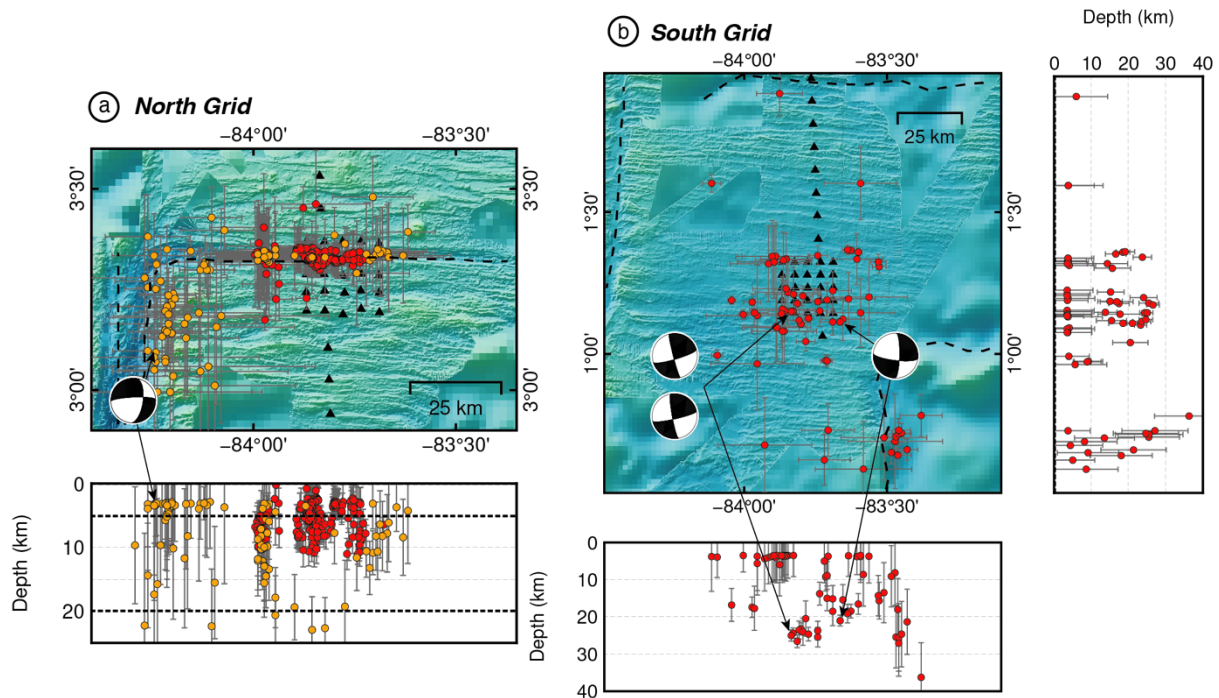
Figure S2. a) Microearthquake locations around the NG showing only events with horizontal uncertainties <±30 km and vertical uncertainties <±15 km for events located outside the network, and with horizontal uncertainties <±20 km and vertical uncertainties <±10 km for events located inside the network. Microearthquakes located with the 1D and 3D velocity models correspond to the orange and red dots, respectively. b) Microearthquake locations around the SG showing only events with horizontal and vertical uncertainties <±20 km. Black triangles indicates the OBS positions. Error bars correspond to event uncertainties calculated from the best-fit ellipsoid of the probability density function of each event.

North Grid

South Grid

Jan 26, 2015, 16:24:21 Jan 31, 2015, 13:18:38 Feb 01, 2015, 10:40:55 Feb 24, 2015, 07:48:22

Jan 29, 2015, 11:08:39 Jan 31, 2015, 14:20:42 Feb 01, 2015, 16:21:07 Feb 24, 2015, 07:58:28

Jan 30, 2015, 07:51:07 Feb 01, 2015, 06:17:50 Feb 01, 2015, 20:57:54 Feb 24, 2015, 15:10:18
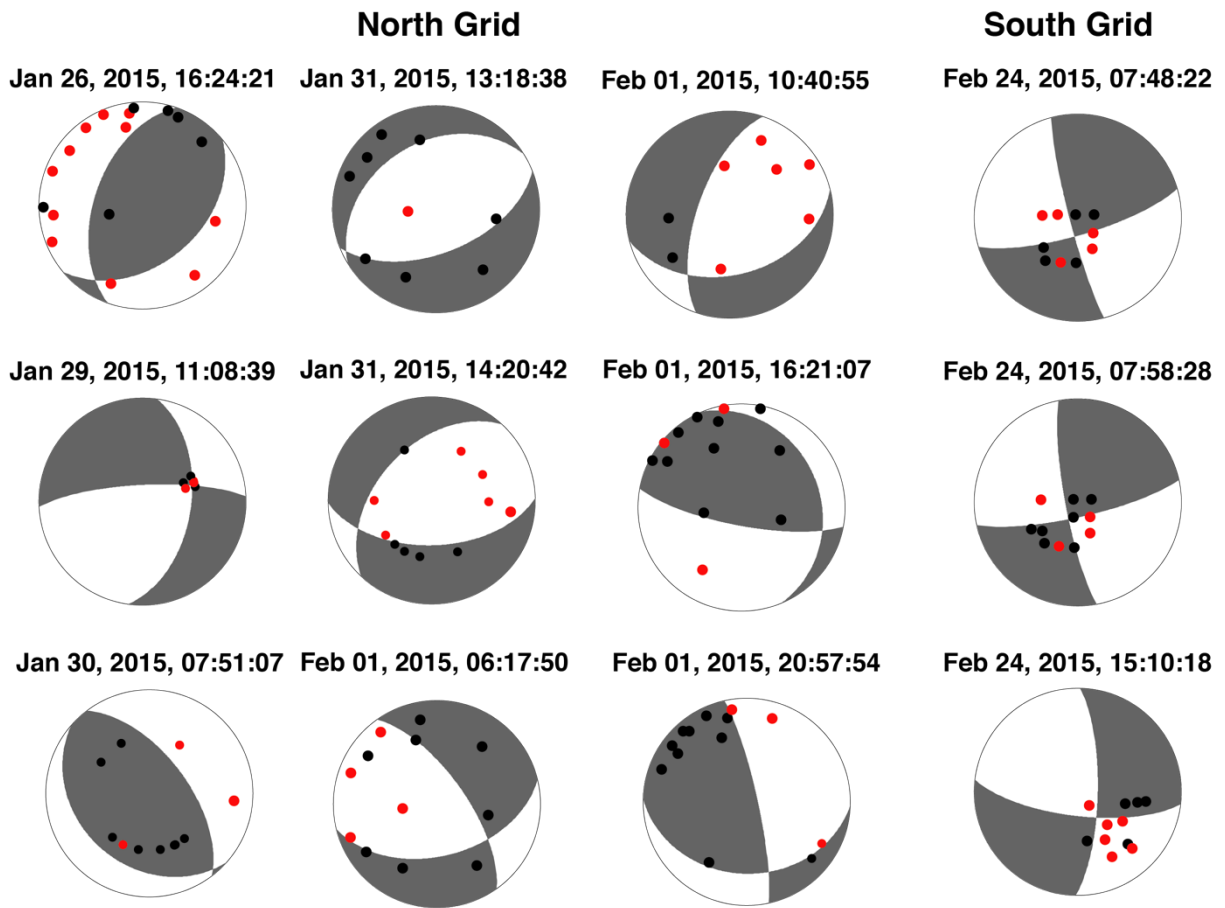
Figure S3. Well-resolved focal mechanism solutions with polarities (red: down, black: up). See Table S1 for the characteristics of each solution.

North Grid

South Grid

Jan 26, 2015, 16:24:21   Jan 31, 2015, 13:18:38   Feb 01, 2015, 10:40:55   Feb 24, 2015, 07:48:22

Jan 29, 2015, 11:08:39   Jan 31, 2015, 14:20:42   Feb 01, 2015, 16:21:07   Feb 24, 2015, 07:58:28

Jan 30, 2015, 07:51:07   Feb 01, 2015, 06:17:50   Feb 01, 2015, 20:57:54   Feb 24, 2015, 15:10:18
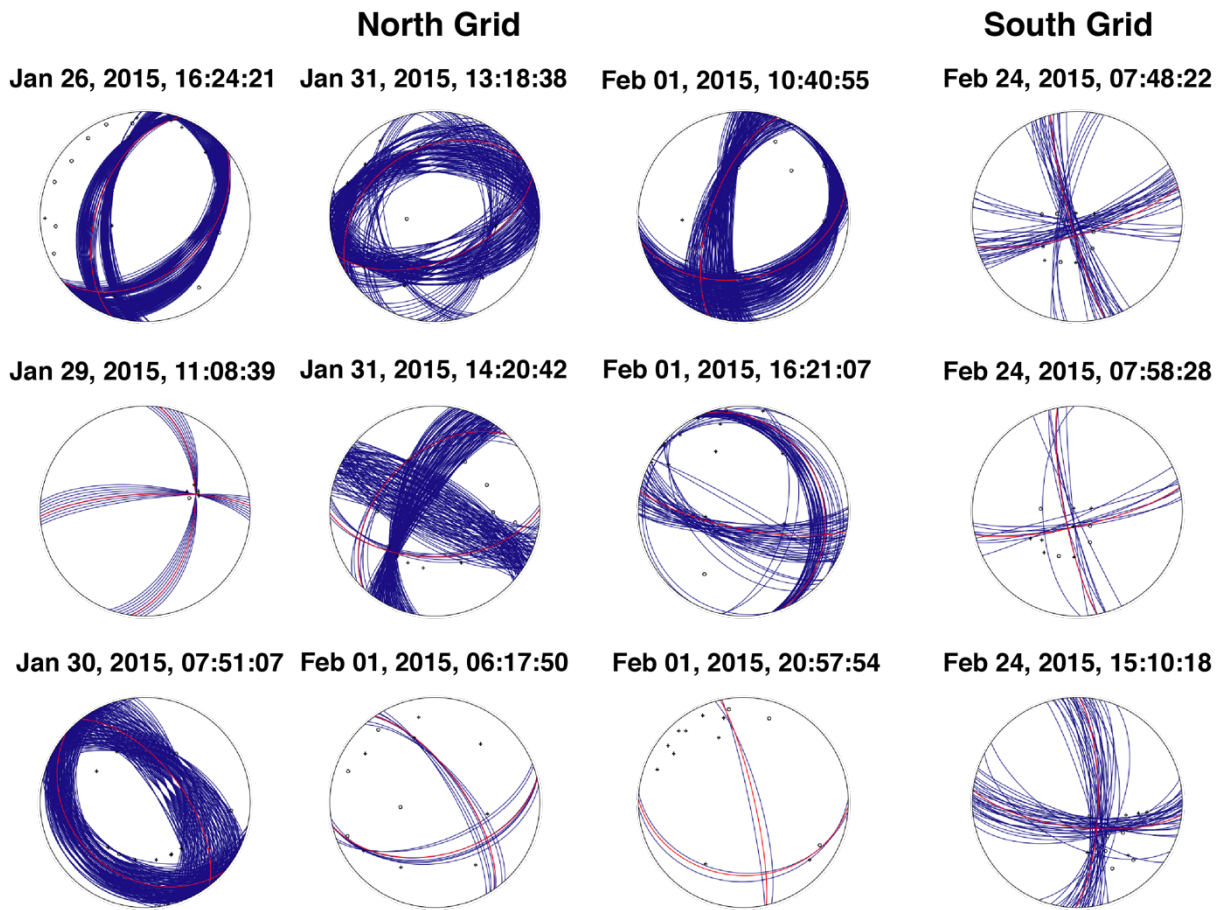
Figure S4. Well-resolved focal mechanism solutions with the final and trial FOCMEC solutions in red and blue, respectively. Polarities are indicated by plus (up) and open circle (down) symbols.
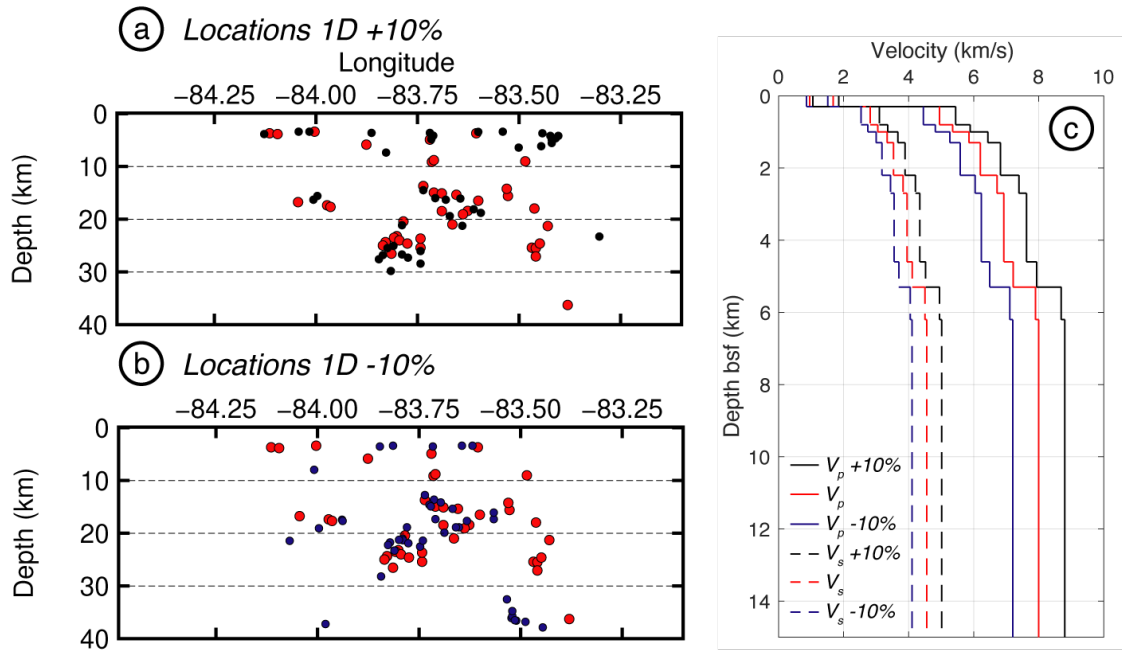
Figure S5. SG microearthquake locations showing only events with horizontal and vertical uncertainties <±10 km with a faster (+10% black dots in a) and slower (-10% blue dots in b) 1D velocity models shown in c). Locations with the intermediate velocity model presented in Figure 5 correspond to the red dots.